A peep into the deep Earth through the stability and compressibility of $RbAlSi_3O_8$ at high pressures and improved temperature measurements within the LHDAC by accounting for wavelength- and temperature-dependent emissivity

Senior Thesis

Submitted in partial fulfillment of the requirements for the
Bachelor of Science Degree
At The Ohio State University

By

Eugenia Hyung
The Ohio State University
2010

Approved by

Wendy R. Panero, Advisor
School of Earth Sciences

Table of Contents

Abstract

The study of the Earth's deep interior relies on knowledge of material behavior under extreme conditions, such as temperatures exceeding 5000 K and pressures up to 3.6 million times the Earth's atmosphere. Physical properties of materials at such conditions can be extrapolated from high-pressure and temperature experiments which can be extended into a depth within the Earth. The laser-heated diamond anvil cell (LHDAC) is one such device that can reproduce the pressures and temperatures of planetary interiors.

^{87}Rb, which decays to ^{87}Sr, serves as a geochemical tracer which is used to determine the age of the continental crust, constrain the age of the Earth's core and to date the age of meteorites. The decay of ^{87}Rb to ^{87}Sr in particular serves as a geochemical tracer for long-lived mantle processes. While Rb in the crust is stored as a feldspar ($RbAlSi_3O_8$), the most abundant mineral of the Earth's crust, the mineral host of Rb in the mantle is uncertain.

Determination of material properties such as the high-temperature equation of state, solid-solid phase transitions, emissivity, and melting curves under deep-Earth conditions is contingent on the ability to accurately measure high temperatures, yet the quality of temperature measurements *in situ* within the LHDAC are hampered by chromatic aberrations introduced by the diamonds and optics of the system. Advances in the design of temperature measurement circumvent chromatic aberrations (Campbell, 2008), such that systematic errors introduced through wavelength-dependent emissivity dominate the errors in the temperature measurement.

Here in this compilation of two projects I report the phase stability and compressibility of a high-pressure polymorph of $RbAlSi_3O_8$, Rubidium-hollandite-I, from LHDAC experiments and wavelength- and temperature-dependent emissivity measurements for various metals including

platinum, tungsten, molybdenum at atmospheric pressure and iron-nickel alloy at 44 GPa as a means to validate temperature measurements. The high-pressure phase diagram of Rubidium feldspar is similar to that of Potassium feldspar, transforming to the hollandite structure at ~15 GPa, then to the hollandite-II structure between 20 to 30 GPa, suggesting that the host minerals for K and Rb in the mantle are identical. The bulk modulus of Rubidium hollandite-I turns out to be 216 (±6) GPa, assuming K'=4. Platinum, tungsten, molybdenum at atmospheric pressure and iron-nickel alloy at 44 GPa display a decrease in wavelength-dependent emissivity for temperatures ranging from 1300K to 3000 K, indicating that corrections are necessary for accurate temperature assessments. Tungsten does not display temperature-dependent emissivity for temperature ranges of 2500 – 2900 K.

Acknowledgements

I owe my gratitude to Sabrina A. R. A. ("Sara") Whitaker for collecting the Rb-hollandite-I data at the National Synchrotron Light Source in Brookhaven and for kindly teaching me how to use Igor to calculate lattice parameters. I also want to thank Dan Reaman for his generosity in providing me with his high-pressure iron-nickel alloy data, and his patience in guiding me through the use of the optics table, Win-Spec and other various lab procedures despite my being "the second-clumsiest person to ever be in the OSU high-pressure mineral physics lab." I am thankful for 2 years of Summer Undergraduate Research Experience (SURE), sponsored by the School of Earth Sciences and Shell, and the two Undergraduate Research Scholarships that I was awarded while at OSU to fund my two projects. I would also like to acknowledge Henry Scott, who has provided the lattice parameter calculator codes, and I am grateful for my colleagues Jason Kabbes and Jeff Pigott for their camaraderie, good sense of humor, and support in times of need. I am also greatly indebted to my advisor, Dr. Wendy R. Panero for her guidance, words of encouragement, patience, and kindness, without whom this thesis and my research would have been impossible. I thank Dad for inadvertently helping me follow through my passion, Mom for supporting me through times of hardship, and last but not least, I fondly extend my gratitude to my Kindergarten teacher, Mrs. Lisberg, who got me hooked on science.

A peep into the deep Earth through the stability and compressibility of $RbAlSi_3O_8$ at high pressures and improved temperature measurements within the LHDAC by accounting for wavelength- and temperature-dependent emissivity

Introduction

Knowledge of the interior of the planet provides information about the composition and structure of the planet as well as the evolutional history of the Earth. Due to the unlikely feasibility of deep-Earth drilling projects extending beyond 10 km (6.4 miles) deep compared to the Earth's radius of 6380 km (4000 miles), scientists have devised various ways to study the Earth's interior through indirect methods. Such methods include inspecting and analyzing mantle xenoliths that have surfaced on the Earth through volcanic eruptions, using seismic waves to probe the Earth, and synthesis of deep Earth conditions through high-temperature and pressure experiments.

The study of the Earth's interior relies on our knowledge of material behavior under extreme conditions with temperatures that range up to 6000 K (10340 °F) and pressures that are up to 3.6 million times the Earth's atmosphere. Indeed, physical properties that have been derived from high pressure and temperature experiments can be extended into any depth within the Earth, where the density and behavior of a material can be extrapolated and assessed. The laser-heated diamond anvil cell (LHDAC) is one such device (Figure 1) that allows for generation of high pressure and temperatures. The LHDAC consists of a cell that contains two small diamonds (~0.3 carats) whose flat, polished tips (surfaces ranging from 0.25 to 0.5 mm in diameter) face each other (Figure 2). High pressures are generated by allowing the force of the screws to be concentrated on the tips of

the diamonds, while temperatures are achieved by means of laser heating on the micrometer-scale sample that is placed between the two diamonds. The structure and density of the material are investigated through analysis of x-ray diffraction patterns.

One aspect of the Earth's interior that sheds insight into the history of the Earth and evolution of the mantle include the chemical abundances of various elements, especially those of K, Rb and Cs (McDonough et al., 1993; Sun, 1982; Hoffmann and White, 1983; Wanke et al., 1984), and the host minerals that are able to encase these elements. The abundances of these alkali metals in the bulk silicate Earth are 240 ppm for K, 0.6 ppm for Rb and 21 ppb for Cs for the Bulk-Silicate Earth, which includes the crust and the mantle (McDonough and Sun, 1995). Knowledge of the physical properties of the host mineral under mantle conditions can address how K, Rb and Cs are retained in the mantle. Most of these elements are concentrated in the crust in the form of feldspar, $XAlSi_3O_8$, where X is one of the alkali elements, generally K or Na, but also can include the less abundant Rb and Cs. Among these radiogenic, alkali elements, ^{87}Rb is a geochemical tracer that can be used to constrain the average age of the Earth's crust (O' Nions et al., 1979). Feldspar and its polymorphs under high pressures as a host mineral of ^{87}Rb are of interest because oceanic lithosphere that holds Rb is capable of being subducted deep into the mantle with parts of feldspar-rich continental crust (Armstrong, 1981; Dupre and Allegre, 1983; Hofmann, 1997; Sobolev and Shasky, 1990). Natural Rb-microcline has been observed to coexist with Potassium microcline in a stoichiometric relationship (Teertstra et al., 1998), and formation of Rb-microcline through exsolution (Teertstra et al. 1998) implies a solvus for the K-Rb feldspar system (Hovis and Roux, 2008).

Numerous equation of state studies relating volume (density) and pressure have been performed for potassium microcline and its high-pressure polymorph in the hollandite structure

(Zhang et al., 1993; Tutti et al., 2001; Sueda et al., 2004; Ferroir et al., 2006). The hollandite structure of $KAlSi_3O_8$ is arranged as a tetragonal crystal phase of the space group I*4*/*m* (Ringwood et al., 1967; Yamada et al., 1984; Zhang et al., 1993) with edge-sharing (Si, Al)O_6 octahedra that form tunnels (Figure 3). These tunnels grant the hollandite structure the capacity to hold large cations such as Cs, Pb, K and Rb (Watanabe and Fujiki, 1986). The hollandite phase of $KAlSi_3O_8$ is stable at pressures greater than ~9 GPa at temperatures of 1000 to 1400 °C (Kinomura et al., 1975; Urakawa et al., 1994; Yagi et al., 1984), and has been shown to transform to the related monoclinic hollandite-II structure of the space group I*2*/*m* at pressures between 28 and 128 GPa and temperatures up to 3650 K (Hirao et al. 2008). Unlike hollandite-I, hollandite-II is unstable at ambient pressure (Sueda et al,. 2004). Although there are no studies on the high-pressure behavior of $RbAlSi_3O_8$ in any phase, it is expected to behave similarly to $KAlSi_3O_8$ because of the similar geochemical properties of K^+ and Rb^+ due to their ionic radii and charge. I expect the polymorphs of $RbAlSi_3O_8$ should exhibit behaviors similar to those of $KAlSi_3O_8$ in terms of compressibility, structural phases, and phase transition.

To determine experimentally the physical properties of materials that belong to the deep Earth hinges on the technical capability to generate and measure accurately high temperatures. Temperatures of samples *in-situ* are measured by fitting the light emitted from the sample to the Planck blackbody radiation curve. While a blackbody, an ideal body that is able to absorb all light and energy, has an emissivity of 1, that of any other object deviates from this ideal value. In high-pressure and high-temperature experiments, the grey-body assumption is employed in temperature measurements, which states that temperature-independent and wavelength-independent emissivity. This ignores possible variables that may affect emissivity, such as composition, molecular and electron transitions, surface quality and emissivity angle.

A current literature assessment (Kavner and Panero, 2004) indicates that wavelength-independent emissivity may well overestimate the temperature by up to 150-200 K if an emissivity decrease of 30% over a 1000 nm range, typical of most metals, is overlooked. Temperature-independent emissivity assumptions cause problems likewise when measuring at temperature gradients. Kavner and Panero (2004) state that an order of magnitude change from 1500-2500 K in temperature-dependent emissivity can lead to an error estimate as much as 70%. Consideration of wavelength-dependent and temperature-dependent emissivity have major implications for accurately assessing temperatures, not only in the realm of high-pressure mineral physics but also in other areas of study, such as condensed matter physics, material science research and synthesis of new materials. There is a potential to detect melting or solid-solid phase transitions in high-pressure experiments through quantifying emissivity changes under different temperature and pressure conditions. The methodology presented in this thesis also opens doors to assessing radiative-heat transfer at the core-mantle boundary, and will be used to reevaluate the nature of high P, T transitions such as those evident in compressibility studies for minerals such as Rb-hollandite-I and hollandite-II by considering temperature conditions in future studies.

Chapter I

Stability and Compressibility of Rubdium-hollandite-I

1.1 Introduction

The hollandite structure is tetragonal, with two axes (*a*) of equal sides and the third of another length (*c*), all configured at right angles. The edge sharing (Si, Al)O_6 octahedral are coordinated through edge-sharing to form tunnels that are parallel to the *c*-axis. The tunneling of the hollandite structure (Figure 3) makes it desirable as a nuclear waste immobilizer and other applications, such as reduction catalysts for NO_x pollutants and fast ion conductors (Fujimoto et al., 2007).

1.2 Methods

1.2.1 Synthesis and Analysis

Rubidium microcline (referred to as Rb-microcline hereafter) was synthesized through ion-exchange methods with powdered Amelia low albite in molten RbCl at 852°C for 216 h and a subsequent 370 h exchange at the same temperature with a different batch of RbCl. This process resulted in a composition of ($Rb_{0.97}Na_{0.01}K_{0.02}Al_{1.01}Si_{2.99}O_8$) (Hovis and Roux, 2008).

A sample of finely powdered Rb microcline was loaded in a diamond anvil cell (DAC) with 3-micron-thick 99.99% pure iron foil serving as a laser absorber. The samples were loaded with 250-500 micron culets in rhenium gaskets pre-indented to ~1GPa. Reported pressures are from the quasi-hydrostatic ruby fluorescence scale (Mao et al., 1986). The samples were compressed to pressures of 15–65 GPa and heated to 2500K with a diode-pumped YLF laser (λ=1053 nm).

Powder x-ray diffraction patterns were collected at room temperature with the LHDAC at the X17C beamline of the National Synchrotron Light Source. X-ray diffraction patterns were collected at the pressure of synthesis and upon decompression to ambient. One sample of Rubidium hollandite-I (Rb hollandite-I hereafter) that was at 20 GPa was recovered and reloaded in silicon oil, and compressed with ~1 GPa steps to ~15 GPa.

1.2.3. Equation of State of $RbAlSi_3O_8$ hollandite

Each X-ray diffraction pattern was manually analyzed by fitting 4 to 11 intensity peaks to Gaussian curves. The peaks from each of the diffraction patterns were indexed and lattice constants were determined by least squares. The isothermal bulk modulus was determined by least squares fitting for the third-order Birch-Murnaghan equation of state,

$$P(V) = \frac{3K_0}{2}\left[\left(\frac{V_0}{V}\right)^{\frac{7}{3}} - \left(\frac{V_0}{V}\right)^{\frac{5}{3}}\right]\left\{1 + \frac{3}{4}(K_0' - 4)\left[\left(\left(\frac{V_0}{V}\right)^{\frac{2}{3}} - 1\right)\right]\right\} \quad (1)$$

where V_0 is the unit cell volume at zero pressure, V the volume at pressure P, K_0 the room temperature bulk modulus, and K_0' the derivative of the room temperature of the bulk modulus. K_0' is fixed at 4 (Figure 6).

1.3 Results

Rb feldspar Rb hollandite-I is stable at experimental conditions up to 20 GPa at 300K. Rb hollandite-II was observed at pressures greater than 30 GPa (Figure 4), putting the range of the phase transition of Rb hollandite-I into hollandite-II at pressures between 20 and 30 GPa. The Rb-hollandite-II phase is not stable at ambient pressure, back converting to the hollandite-I phase.

The cell parameters obtained by least-square fitting of the XRD data at zero pressure and room temperature were; a = 9.42 Å, c = 2.74 Å, and V = 243.23 Å^3. The isothermal bulk modulus of Rb hollandite-I at 300K was calculated to be 216.06 (4) GPa when K_0' is fixed to 4.0 (Figure 5). The lattice a to c ratio of Rb-hollandite-I was shown to decrease overall with increasing pressure increase.

1.4 Discussion

The bulk modulus of Rb-hollandite-I at 216.06 (4) GPa shows that the Rb-hollandite-I structure is stiffer than the structure of K-hollandite-I when compared with the reported results from existing literature. Zhang et al. (1993) and Ferroir et al. (2006) report the bulk modulus of K-hollandite-I to be 180(3) GPa and 201.4(7) GPa, respectively. Zhang et al. discusses the effects of constraining V_0. The bulk modulus of K-hollandite-I is sensitive to the constraint of V_0, and produces a bulk modulus of 191(3) GPa, which is significantly different when not constrained (Zhang et al., 1993). This is also observed for Rb-hollandite, which reveals a bulk modulus of 206.65(6) when V_0 is not constrained. It is recommended that V_0 be constrained when deriving the equation of state (Jeanloz and Hazen, 1991).

Different values of V_0 were retrieved for rubidium hollandite-I for various conditions. While this may be a reflection of analytical error, it is also possible that the different values of the unit cell volume at 0 GPa may reflect uptake of Fe from conditions in which Rb-hollandite was synthesized in the study. Another possible explanation for the variations in the values may lie in the deviations of ordering of (Si, Al)O_8 octahedral, due to various internal energy states. The sensitivity of the bulk-modulus to V_0 may be a reflection of how small-scale structural variations can affect the overall compressibility and behavior of a mineral.

The hollandite structure and behavior of $RbAlSi_3O_8$ can be seen as analogous to $KAlSi_3O_8$. The *a* lattice value for K-hollandite is 9.33 Å while the value of lattice *c* is 2.73 Å (Ferroir et al. 2006). Substitution of the K^+ by Rb^+ results in an increase in both these lattices, but one that is exaggerated for lattice *a* when compared with the change of lattice *c*. Comparison of the lattice constants *a* and *c* of Rb-hollandite of 9.42 Å and 2.74 Å, respectively, shows there is a 0.96% increase for the *a* lattice and a 0.47% increase for that of *c*. The *a*/*c* ratio (Figure 6) decreases for both the K- and Rb-hollandite-I structures with increasing pressure, showing preferential compression in the *a* axis direction to due to tunnels made by edge sharing (Si, Al)O_6 octahedral.

The similar bulk moduli, lattice parameters, and the K/Rb ratio in the mantle which ranges from 250 to 290 (Weaver and Tarney, 1984; Taylor and McLennan, 1985), imply that Rb is not likely to affect the structure of hollandite-I significantly when in solid solution with K, as (K, Rb)$AlSi_3O_8$-hollandite.

Chapter II

Improved Temperature Measurements by Accounting for Wavelength-Dependent and Temperature-Dependent Emissivity

2.1 Introduction

Temperature measurements for the LHDAC are done using spectroradiometry. This method uses Planck's law, which states that a blackbody, an idealized body that is able to absorb all light shone upon it, emits electromagnetic waves in a predictable pattern that can be modeled into Planck's blackbody radiation curve for all wavelengths, according to the corresponding temperature of the object. By assuming blackbody radiation, the temperature of an object can thus be measured by recording and plotting these intensities of light versus wavelength. In reality, any kind of object reflects some kind of light, which deviates from ideality. A common engineering assumption that is made in LHDAC temperature measurements is that emissivity is constant for all wavelengths and temperatures. This is shown to be potentially problematic in temperature measurements as assessed in Kavner and Panero (2004).

The intensity of light is modeled on Planck's blackbody radiation curve which is a function of temperature and wavelength:

$$I(\lambda, T) = \varepsilon(\lambda, T) \frac{2\pi hc^2}{\lambda^5 (e^{\left(\frac{hc}{\lambda kT}\right)} - 1)} \qquad (2)$$

where I is the intensity of light emitted from the material dependent on λ (wavelength) and T (temperature), and ε (emissivity) (Figure 7). Emissivity is dependent on variables such as temperature, emissivity angle, wavelength, and individual properties of the material such as reflectivity and smoothness of surface.

2.2 Methods

2.2.1 Wavelength Dependent Emissivity through Wien's Approximation

With Wien's approximation to Planck's Law ($e^{hc/\lambda kT} >> 1$), the relationship between normalized intensity ($J = \ln(I\lambda^5)$) and normalized frequency ($\omega = -hc/\lambda k$) can be expressed linearly, assuming constant emissivity (Jeanloz and Heinz, 1984; Heinz and Jeanloz, 1987). Taking the natural log over both sides of equation (2), we get a linear equation such that:

$$\ln[I(\lambda,T)] = \ln[\varepsilon(\lambda,T)\frac{2\pi hc^2}{\lambda^5\left(e^{\left(\frac{hc}{\lambda kT}\right)}\right)}] \qquad (3)$$

$$\ln[I(\lambda,T)] = \ln[\varepsilon(\lambda,T)] + \ln(\frac{2\pi hc^2}{\lambda^5}) - hc/\lambda kT. \qquad (4)$$

The resulting equation can be simplified and expressed in terms of $y = ax + b$ where J would be analogous to y, and $\omega \equiv -hc/\lambda k$ to x.

$$J = (1/T)\omega + b \qquad (5)$$

From this approximation, we can derive that the inverse of the slope of the equation is the temperature of the material at hand (Figure 8). Curvatures in the slope would be indicators of wavelength dependent emissivity.

2.2.2 Wavelength-Dependent Emissivity through Two-color Pyrometry

Two-color pyrometry is an expression of a series of temperatures, which are calculated from pairs of intensities separated by a fixed spectral difference, $\omega_1 - \omega_2$:

$$T = \frac{\omega_2 - \omega_1}{J(\omega_2) - J(\omega_1)} \qquad (6)$$

(Kavner and Panero, 2004). The results are plotted to show temperature versus wavelength for the analysis range. For constant wavelength-dependent emissivity, the plotted temperatures for the range of wavelengths would be consistent for all intervals of analysis. Changes in temperature along the plot are either an indicator of changes in wavelength-dependent emissivity or noise (Figure 9).

2.2.3 Temperature-Dependent Emissivity

The total light intensity emitted by the sample is a strong function of temperature:

$$\int_0^\infty I(\lambda, T)\, d\lambda = \varepsilon(T)\sigma T^4 \tag{10}$$

where σ is the Stefan-Boltzmann constant = 5.67×10^{-8} $W/m^2/K^4$.

The relative temperature-dependent emissivity is derived as a ratio of the intensity of light at a certain wavelength that is assumed to be wavelength-independent to the spectra, corrected for system response that:

$$\varepsilon(T) = \int (I_{measured}) d\lambda / \int (I_{Planck} * (I)) d\lambda \tag{11}$$

The light intensities emitted by a hot metal wire were filtered through cellophane 10 nm band-pass filters centered at wavelengths of 500nm, 600nm, 700nm, 800nm and 900nm. The spectra were collected with an SP150 spectrometer with a 100 μm entrance slit and PIXIS 100 CCD. The temperature assessed from the spectrometer was then compared with the light intensities collected for different wavelengths at the same current (temperature).

2. 2. 4 Experiment

In order to obtain wavelength-dependent and temperature-dependent emissivity data for various metals, a light bulb (Figure 10) was modeled and built after the geometry of a diamond anvil cell. The light bulb incorporates an exchangeable filament and allows for nitrogen or argon flow to prevent the metal from reacting with oxygen.

A neon penlight was first placed at the position of the light bulb to calibrate wavelength. A calibrated quartz-tungsten Oriel lamp light source was used to measure the spectral response of the optical system. The current that flows through the filament acted as a control to vary the temperature.

The experiments consisted of taking neon lamp calibrations and using the Oriel quartz lamp to measure system response every time the SP150 spectrometer was turned on. Various metal wires such as platinum, tungsten, molybdenum and iron-nickel alloy, were the filament of the light bulb. The intensity of the light radiated from the heated wire through a filter of a certain wavelength was fitted with the Planck blackbody radiation curved to find the wavelength-dependent and temperature-dependent emissivity for the metals using Wien's approximation and two-color pyrometry. The voltage was adjusted to control the temperature of the wire, while the temperature was measured by fitting the overall intensity of light emitted from the wire to the Planck's Law.

2. 3 Results

Molybdenum wire at 0 GPa shows a decrease in wavelength-dependent emissivity at higher wavelengths at temperature ranges of 1100 K to 3100 K by up to 25%. Tungsten wire data collected at 0 GPa also show a gradual decrease in emissivity with increase in wavelength between the

temperature ranges of 2000 K to 2800 K by up to 20%, with the effect more accentuated at higher temperatures. Emissivity measurements of Fe-Ni alloy in the LHDAC at 44 GPa and 1150 K–2000 K show a decrease in emissivity by up to 50% at higher wavelengths over a wavelength range of 640 nm to 760 nm. The wavelength-dependent emissivity of platinum for the temperature ranges of 1300 K to 2050 K at 0 GPa shows that the emissivity for platinum is almost constant over the analysis range of 600 to 900 nm.

Temperature-dependent emissivity data for tungsten wire from 2500 K to 2900 K at 0 GPa show that tungsten exhibits no temperature-dependent emissivity for this analysis range (Figure 12).

2. 4 Discussion

A drawback of the two-color pyrometry method is that the analysis is sensitive to noise and small errors in system response. Two-color pyrometry plots often display background noise and system response that has not been fully corrected for, which make it hard to determine accurately minute emissivity changes over a range of wavelength that don't display a trend. Only wavelength-dependent emissivity shows a trend with wavelength.

Molybdenum and tungsten are likely to be subject to temperature corrections, while the steady consistency of wavelength-dependent emissivity over the 600–900 nm range for platinum shows that the difference between the actual temperature and the measured temperature of platinum at temperature ranges of 1300-2050 K will be minor. As tungsten does not show temperature-dependent emissivity for the temperature ranges of 2500–2900 K, it will not be subject to adjustment for the aforementioned temperatures in measuring temperature gradients. While the decrease in wavelength-dependent emissivity at 44 GPa for Fe-Ni for the temperature measurements

signifies that major adjustments will have to be made, curves in the Fe-Ni alloy data at 2000 K exhibit system-response in the data.

While the majority of heat in the Earth's mantle is transported through advection, increasing attention has been paid in recent years to the likelihood that other heat transfer mechanisms can play a significant role, one such example being radiative heat transfer (Goncharov et al., 2008; Keppler et al., 2008).

Radiative thermal conductivity is expressed in terms of:

$$k_R = \frac{16n^2\sigma T^3}{3\alpha_R} \quad . \qquad (11)$$

The Rosseland coefficient, defined such that:

$$\frac{1}{\alpha_R} = \frac{\int_0^\infty \frac{1}{\alpha(\nu)} \frac{de(\nu,T)}{dT} d\nu}{\int_0^\infty \frac{de(\nu,T)}{dT} d\nu} \qquad (12)$$

where $e(\nu, T)$ is the Planck blackbody radiation curve, and $a(\nu)$ the measured absorption coefficient, is highly dependent on the frequency of maximum radiation (Rosseland, 1924; Siegal and Howel, 1992).

Recent papers such as Keppler et al. (2008) discuss the effect of radiative thermal conductivity of various materials pertaining to the lower mantle assuming blackbody radiation which discounts the effects of emissivity. It is possible that the effect of radiative thermal conductivity is overplayed in this respect, especially for lower range temperatures where emissivity is smaller, as shown in studies for metals such as tungsten and molybdenum (Touloukian and Ho, 1979). Through reference to emissivity "standards" as established here, the relative emissivity of deep-Earth materials can be determined to constrain the absolute value of emissivity. Temperature-

dependent and wavelength-dependent emissivity will affect the frequency of maximum radiation. Further modeling and analysis will need to be done to assess these issues quantitatively.

References

Allan, D. R., and R. J. Angel. (1997) A high-pressure structural study of microcline ($KAlSi_3O_8$) to 7 GPa. *Eur. J. Mineral.* 1997, Vol. 9, pg 263-275

Ferroir, T., T. Onozawa, T. Yagi, S. Merkel, N. Miyajima, N. Nishiyama, T. Irifune, and T. Kikegawa. (2006) Equation of state and phase transition in KAlSi3O8 hollandite at high pressure. *American Minerologist*, Vol. 91, pg. 327-332.

Fufimoto, K., K. Takamori, and S. Ito. (2007) Structure and property of Hollandite-type $K_xM_xSn_{8-x}O_{16}$ (M; Ga and Fe, x-2) single crystal. *Acta Cryst.* A63, s217

Gast, P. W. (1960) Limitations on the Composition of the Upper Mantle. *Journal of Geophysical Research* Vol. 65, pg. 1287-1297.

Goncharov, A. F., B. D. Haugen, W. Struzhkin, P. Beck, and S. D. Jacobsen. (2008) Radiative conductivity in the Earth's lower mantle. *Nature,* Vol. 456 pg. 231-234

Guy, H. L. and J. Roux, (2008) Thermodynamic mixing properties of Rb-K feldspars. *American Minerologist*, Vol. 93, pg. 1597-1602, 2008

Heinz, D. L. and R. Jeanloz (1987), Temperature measurements in the laser-heated diamond anvil cell. In: Maghnani, M., Syono, Y. (Eds.), High-pressure Research in Mineral Physics. *American Geophysical Union*, Washington, DC, pg. 113-127

Hirao, N., E. Ohtani, T. Kondo, T. Sakai, and T. Kikegawa. (2008) Hollandite II phase in $KAlSi_3O_8$ as a potential host mineral of potassium in the Earth's lower mantle. *Physics of the Earth and Planetary Interiors*. Vol. 166, pg. 97- 104

Hofmann, A. W. and W. M. White. (1983) Ba, Rb and Cs in the Earth's mantle. *Z. Naturforsch.* Vol. 38, pg. 256-266

Jeanloz, R., and R. M. Hazen. (1991) Finite-strain analysis of relative compressibilities –application to the high-pressure wadsleyite phase as an illustration. *Am. Mineral.*, Vol. 76, pg. 1765-1768

Jeanloz, R., and D. L. Heinz. (1984) Experiments at high temperature and pressure-laser heating through the diamond-cell experiments. *Phil. Trans. R. Soc. Lond.*, Ser. A: Math. Phys. Eng. Sci., Vol. 354, pg. 1279-1305

Kavner , A. and W. R. Panero. (2004) Temperature gradients and evaluation of thermoelastic properties in the synchrotron-based laser-heated diamond cell, *Phys. Earth Planet. Int.*, *143-144*, 527-539

Keppler, H., L.S. Dubrovinsky, O. Narygina and I. Kantor. (2008) Optical absorption and radiative thermal conductivity of silicate perovskite to 125 gigapascals. *Science*, Vol. 322, pg. 1529-1531

Kinomura, N., S. Kume and M. Koizumi. (1975) Stability of K2Si4O9 with wadeite type structure, paper presented at 4th International Conference on High Pressure, Int. Assoc. for the Adv. Of High Pressure and Technol., Kyoto, Japan.

Mao, H. K., Xu, J., and Bell, P. M. (1986) Calibration of the ruby pressure gauge to 800 kbar under quasi-hydrostatic conditions. *Journal of Geophysical Research*, Vol. 91, pg. 4673- 4676

McDonough, W. F., S.-s. Sun, A. E. Ringwood, E. Jagoutz, and A. W. Hofmann. (1992) Potassium, rubidium and cesium in the Earth and Moon and the evolution of the mantle of the Earth. *Geochimica et Comochimica Acta,* Vol. 56, pg. 1001-1012.

McDonough, W. F., and S.-s. Sun. (1995) The composition of the Earth. *Chemical Geology*, Vol. 120 pg. 223-254

O'Nions., R. K., N. M. Evensen and P. J. Hamilton. (1979) Geochemical Modeling of Mantle Differentiation and Crustal Growth. *Journal of Geophysical Research.* Vol. 84, pg. 6091-6101

Ringwood, A. E., Reid, A. F., Wadsley, A. D. (1967) High-pressure $KAlSi_3O_8$, an aluminosilicate with sixfold coordination. *Acta Cryst.* Vol. 23, pg. 1093-1095.

Rosseland, S. (1924) Electrical state of a star. *Mon. Not. R. Astron. Soc.*, Vol. *84*, pg. 720-728

Siegal J. and J. R. Howell, *Thermal Radiation Heat Transfer*, Taylor and Francis, Washington, DC, 1992

Sun, S.-S. (1984) Geochemical characteristics of Archaean ultramafic and mafic volcanic rocks: Implications for the mantle composition and evolution. In *Archaean Geochemistry* (ed. A. K. Kroner et al.), pg. 25-46. Springer-Verlag.

Taylor S. R. and S. M. McLennan. (1985) *The Continental Crust: its Composition and Evolution.* Blackwell. 1985

Teertstra, D. K., P. Cerny, and F. C. Hawthorne. (1997) Rubidium-rich feldspars in a granitic pegmatite from the Kola Peninsula, Russia. *The Canadian Mineralogist.* Vol. 35, pg. 1277-1281

Touloukian, T. S. and C. Y. Ho (Eds), *Thermophysical Properties of Matter,* Plenum Press, New York, 1979.

Tutti, F., L. S. Dubrovinsky, S. K. Saxena. (2001) Stability of $KAlSi_3O_8$ hollandite-type structure in the Earth's lower mantle conditions. *Geophys. Res. Letters.* Vol. 28, pg. 2735-2738

Urakawa, S., T. Kondo, N. Igawa, O. Shimomura and H. Ohno. (1994) Synchrotron transition study on the high-pressure and high-temperature phase relations of KAlSi3O8. *Phys. Chem. Miner.*, Vol. 21, pg. 387 –391

Wanke, H., G. Dreibus, and E. Jagoutz. (1984) Mantle chemistry and accretion history of the earth. In *Archaean Geochemistry* (ed. A. Kroner et al.) pg. 1-24. Springer-Verlag.

Watanabe M. and Y. Fujiki. (1986) The Effects of Cation Substitution on the Hollandite-Type Structure. *Journal of Solid State Chemistry*. Vol. 66, pg. 56-63

Weaver B. L. and J. Tarney. (1984) Major and trace element composition of the lithosphere. *Physics and Chemistry of the Earth*. Vol 15, pg. 39-68

Yagi A., T. Suzuki, and M Akaogi. (1994) High pressure transitions in the system KAlSi3O8 – NaAlSi3O8. *Phys. Chem. Miner.*, Vol. 21, pg. 12-17

Yamada, H., Matsui, Y., Ito, E., (1984) Crystal-chemical characterization of $KAlSi_3O_8$-$NaAlSi_3O_8$. *Phys. Chem. Minerals*. Vol. 21, pg. 12-17

Zhang, J., J. Ko, R. M. Hazen, and C. T. Prewitt. (1993) High-pressure crystal chemistry of KAlSiO8 hollandite. *American Mineralogist*, Vol. 78, pg. 493-499.

Appendix: Figures

Figure 1. Laser-heated diamond anvil cell (LHDAC), which measures about 3 inches in diameter and 2 inches tall.

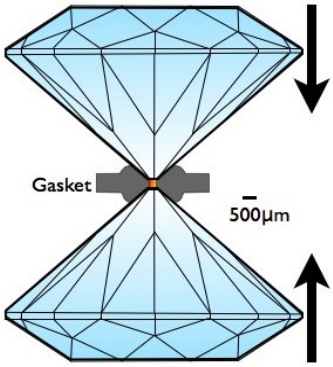

Figure 2. Diamond and sample set-up within the LHDAC.

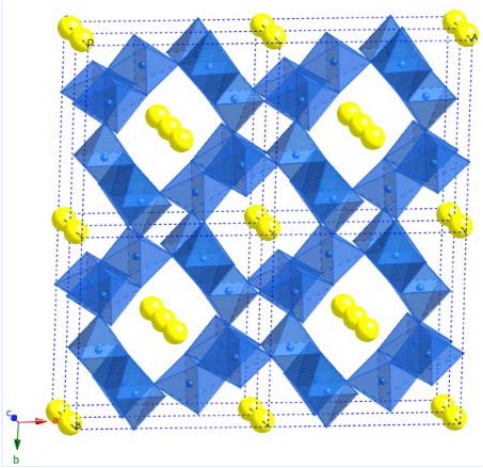

Figure 3. Tunneling of the hollandite structure in the direction of the *c*-axis through edge-sharing (Si, Al)O_8 octahedra. (Si, Al)O_8 octahedra are represented by the blue polyhedra, while the site for +1 charge cations is represented with yellow balls. The smaller blue balls represent either Si or Al.

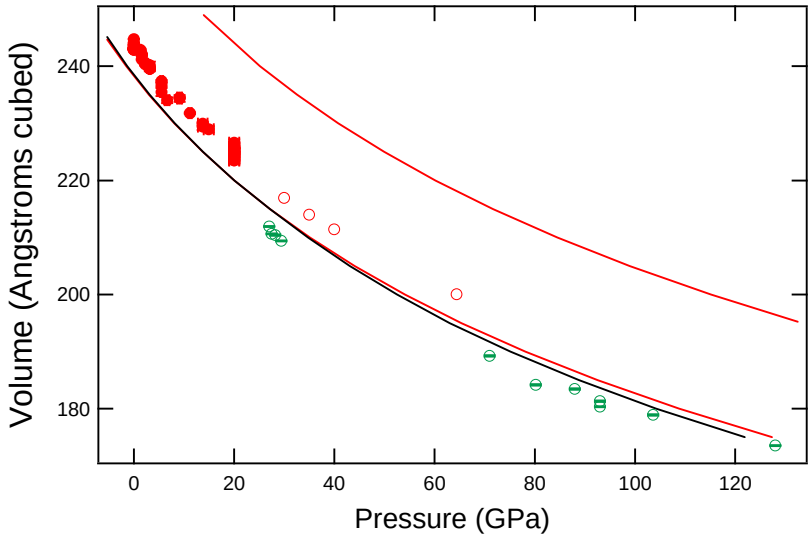

Figure 4. Rb-hollandite-II (red open circles) alongside Rb-hollandite-I (closed red circles) and K-hollandite-II (open green circles; from Ferroir et al. 2006)

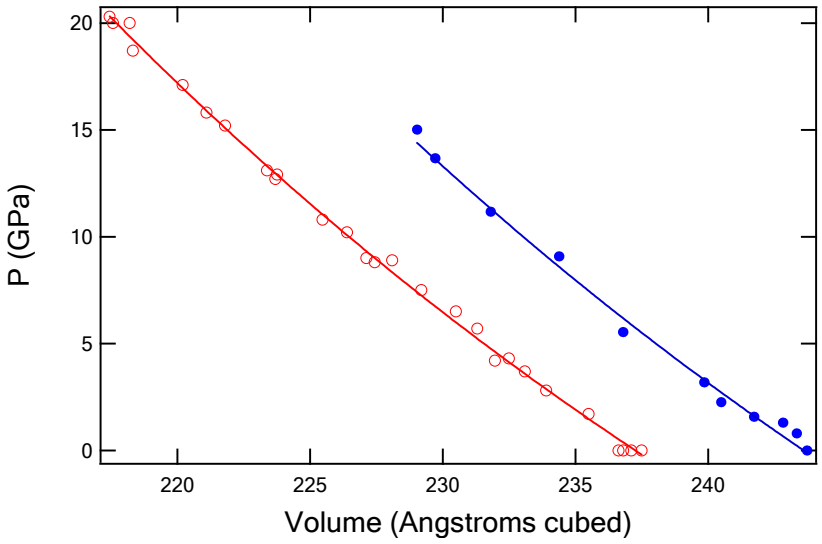

Figure 5. Rb-hollandite data plotted pressure vs. volume (blue, closed circles) with K-hollandite data (red, open circles; from Zhang et al., 1993 and Ferroir et al., 2006). Both are fitted to the Birch-Murnagan 3rd order equation of state.

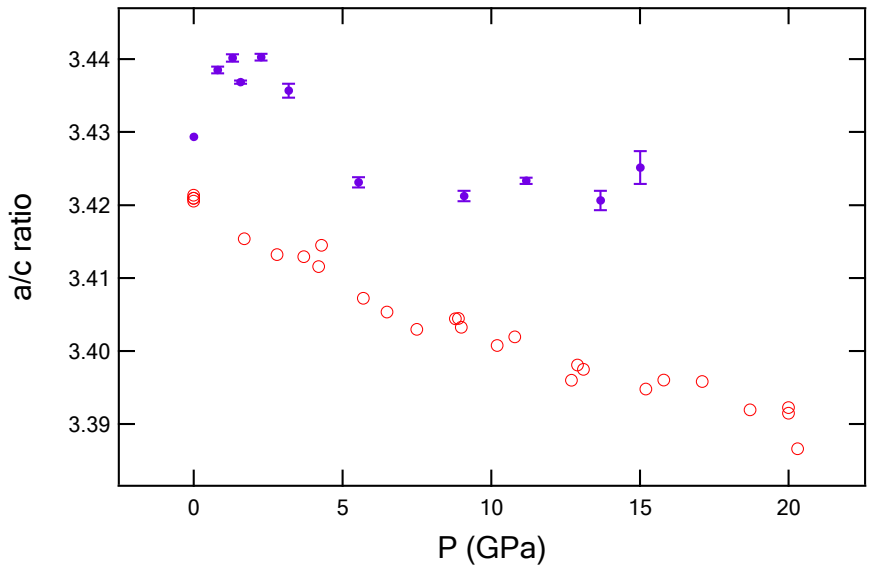

Figure 6. Trend of *a*/*c* ratio with increasing pressure for Rb-hollandite-I (purple, closed circles) and K-hollandite-I (red, orange circles; from Zhang et al., 1993 and Ferroir et al., 2006)

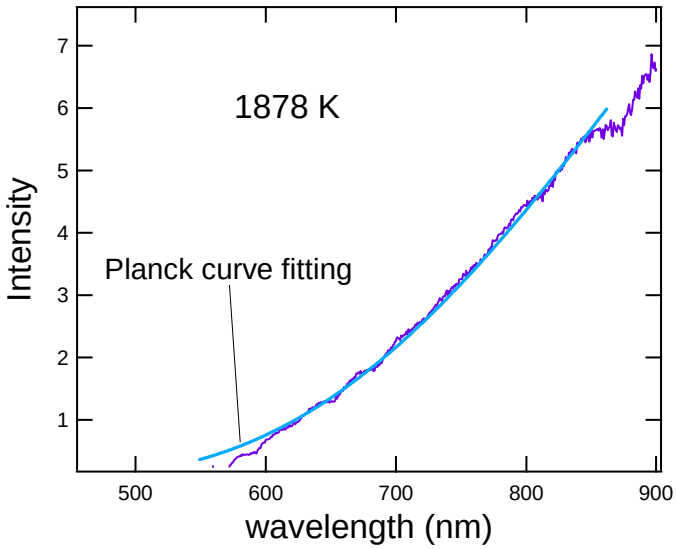

Figure 7. Planck curve fitting for Molybdenum. Analysis reveals the temperature to be 1878 K.

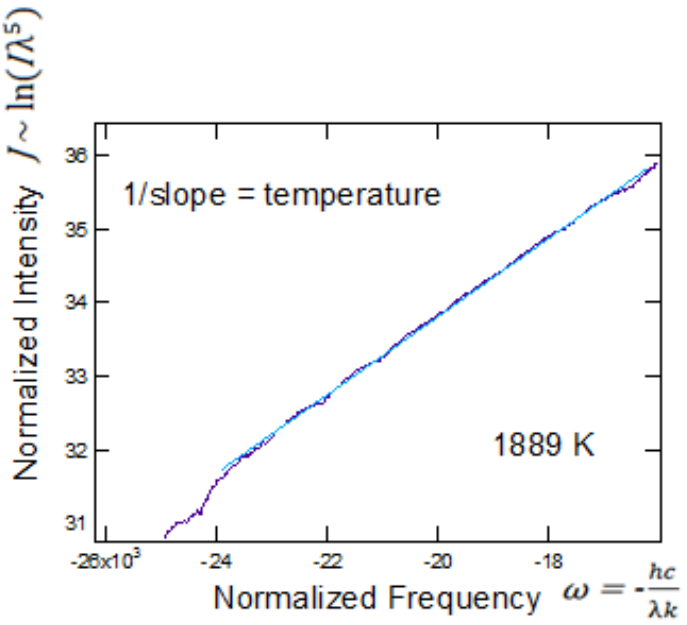

Figure 8. Wien frequency fitting for molybdenum. This analysis reveals the temperature to be 1889 K.

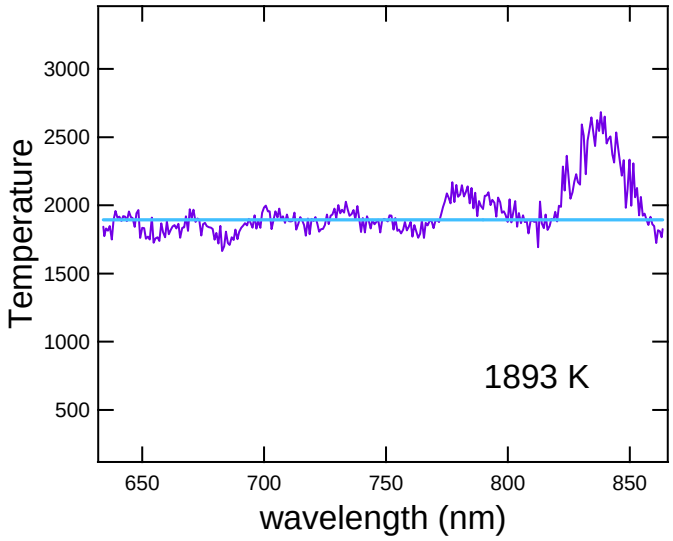

Figure 9. Two-color pyrometry plot for molybdenum. Analysis reveals the temperature to be 1893 K. Figure displays background noise and system response.

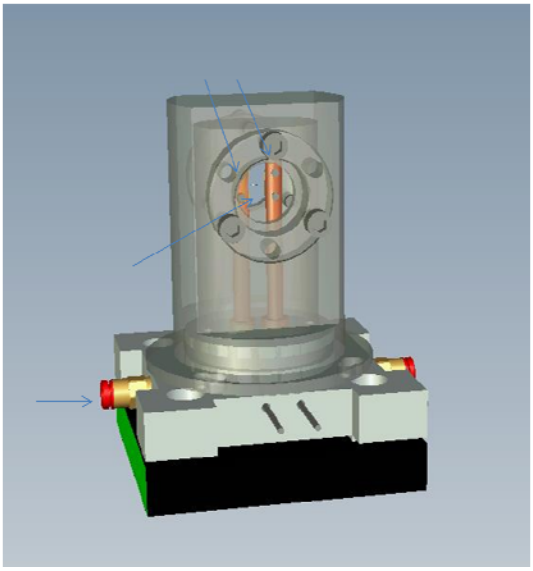

Figure 10. Light bulb modeled after the geometry of the LHDAC

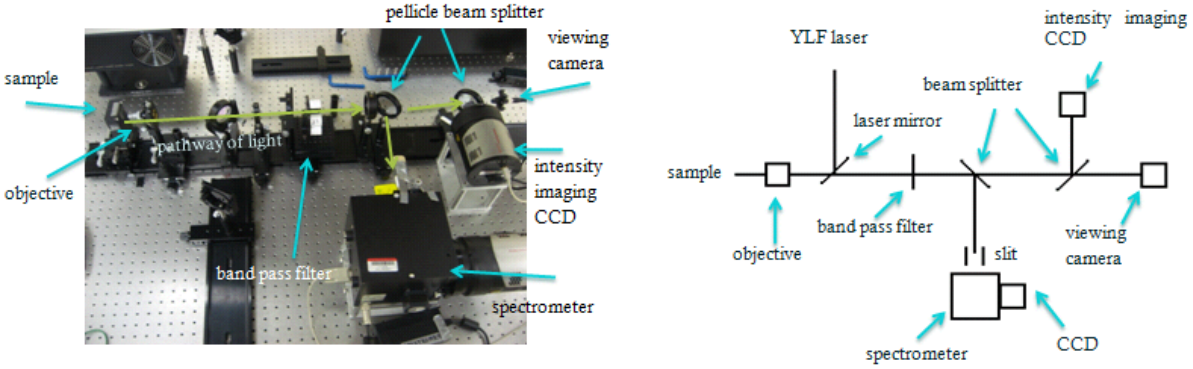

Figure 11. Laser-heating optics table in the high-pressure mineral physics lab at Ohio State University (left) and schematics of optics table (right)

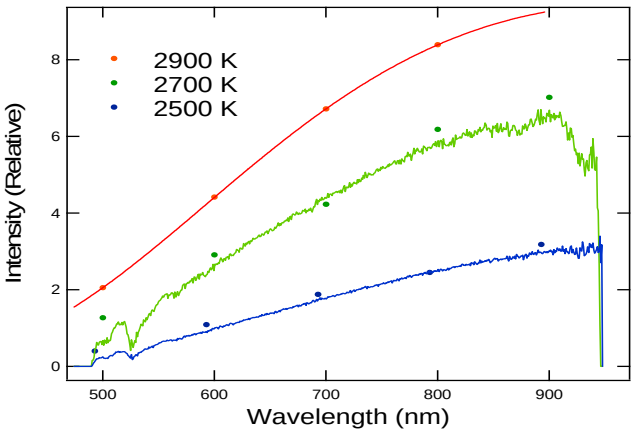

Figure 12. Temperature-dependent emissivity measurements for tungsten at 2500 K – 2900 K. The lines represent data collected with the spectrometer while the dots represent data collected for a band of wavelength with the image intensity CCD.